TECHNICAL ARTICLE

Characterization and Rietveld refinements of new dense ceramics $Ba_{3-x}Sr_xTb_{3-x}Ce_xO_9$ ($x = 1$ and 1.5) perovskites

Yali Su,[1,2] Dayong Lu ⓘ,[1,a)] and Shan Wang[1]
[1]*Key Laboratory for Special Functional Materials in Jilin Provincial Universities, Jilin Institute of Chemical Technology, Jilin 132022, China*
[2]*College of Chemistry, Jilin University, Changchun 130012, China*

$Ba_{3-x}Sr_xTb_{3-x}Ce_xO_9$ ($x = 1$ and 1.5) ceramics (BSTC) with a relative density of 93% and a grain size distribution of 0.2–3 μm were prepared by the mixed-oxides reaction route. The crystalline structures, microstructures, valence states, and electrical properties of two ceramics were analyzed using X-ray powder diffraction (XRPD), scanning electron microscopy (SEM), X-ray photoelectron spectroscopy (XPS), electron paramagnetic resonance (EPR), and electrical measurements. Rietveld analyses of XRPD patterns show that BSTC1 is indexed as a trigonal structure with the space group *R*-3*c*, and BSTC3/2 is indexed as an orthorhombic perovskite structure with the space group *Pmcn*. The EPR, XPS, and electrical conductivity results confirm that Ce and Tb ions in BSTC exist as Ce^{4+} and mixed-valence states of Tb^{4+}/Tb^{3+}, respectively. At room temperature, the two BSTC ceramics exhibit a similar semiconducting behavior. The relationships between electrical conductivity and temperature/frequency are provided. The defect chemistry is discussed. © 2020 International Centre for Diffraction Data. [doi:10.1017/S0885715620000056]

I. INTRODUCTION

Perovskite-type oxides, such as $BaCeO_3$ and $SrCeO_3$, are state-of-the-art high-temperature proton conductors as electrolytes in solid oxide fuel cells (SOFC) because of its high protonic conductivity when exposed to a humidified hydrogen-containing atmosphere at temperatures higher than 300 °C (Uchida *et al*., 1983; Scherban *et al*., 1988; Iwahara *et al*., 2004; Tolchard and Grande, 2007; Fu and Weng, 2014; Knight *et al*., 2015). In order to improve proton conductivity, several kinds of rare-earth-doped $BaCeO_3$ and $SrCeO_3$ ceramics have been developed: (1) $BaCe_{1-x}RE_xO_{3-\delta}$, via the B-site replacement of Ce^{4+} by acceptor-type trivalent rare-earth ions (RE^{3+}) such as $RE^{3+} = Y^{3+}$, Pr^{3+}, Nd^{3+}, Sm^{3+}, Gd^{3+}, Eu^{3+}, Tb^{3+}, and Yb^{3+} (Matsumoto *et al*., 1999; Wang *et al*., 2004; Wu *et al*., 2004; Sharova *et al*., 2005; Malavasi *et al*., 2008); (2) $Ba(Ce_{0.8-y}Pr_yGd_{0.2})O_{2.9}$, via the B-site co-doping with double rare-earth ions Pr^{3+} and Gd^{3+} (Mukundan *et al*., 2001); and (3) $BaCe_{0.2}Zr_{0.7}RE_{0.1}O_{3-\delta}$, via the B-site co-doping with Zr^{4+} and RE^{3+} ($=Y^{3+}$, Sm^{3+}) (Barison *et al*., 2008; Ricote *et al*., 2012; Kannan *et al*., 2013; Choi *et al*., 2014). A more complex system $Ba_{1-x}Sr_xCe_{0.5}Zr_{0.35}Y_{0.1}Sm_{0.05}O_{3-\delta}$ with a cubic perovskite structure (the space group *Pm*-3*m*), in which Sr^{2+} and $Zr^{4+}/Y^{3+}/Sm^{3+}$ are incorporated into the A- and B-sites in $BaCeO_3$, respectively, shows high conductivity and high-density proton conductivity (Radenahmad *et al*., 2016). From another perspective, the commercial application of materials has been hindered by the technical difficulty of

creating fully dense ceramics with good mechanical properties (Dahl *et al*., 2007). Thus, dense $SrCeO_3$- or $BaCeO_3$-based ceramics with simultaneous occupations of both the A- and B-sites may be promising candidates for high-temperature proton conductors in SOFC.

In this work, two ceramics with nominal compositions $Ba_{1-x/3}Sr_{x/3}Tb_{1-x/3}Ce_{x/3}O_3$ ($x = 1$ and 1.5) (BSTC) were prepared using the mixed-oxides method. The refined crystal structures of BSTC are identified using Rietveld refinements. They exhibit higher densification and have perovskite structures with the general formula $Ba_2SrTb_2CeO_9$ and $Ba_{1.5}Sr_{1.5}Tb_{1.5}Ce_{1.5}O_9$, similar to $Sr_2CaFe_2WO_9$ and $Sr_2PbFe_2TeO_9$ perovskites, respectively (El Hachmi *et al*., 2018). Scanning electron microscopy (SEM), X-ray photoelectron spectroscopy (XPS), electron paramagnetic resonance (EPR), and electrical measurements were employed to discuss the crystalline structure and valence states of rare-earth ions Ce and Tb.

II. EXPERIMENTAL

A. Synthesis

Ceramic raw materials were reagent-grade $BaCO_3$ (99.5%), $SrCO_3$ (99.5%), Tb_4O_7 (99.9%), and CeO_2 (99.9%) powders. Two ceramics were prepared according to the nominal formulas of $Ba_{1-x/3}Sr_{x/3}Tb_{1-x/3}Ce_{x/3}O_3$ ($x = 1$ and 1.5) (abbreviated as BSTC1 and BSTC3/2, respectively) using a conventional mixed-oxides method. The stoichiometric mixtures in accordance with the above metal ratios Ba:Sr:Tb:Ce were carefully ground in an agate mortar, and then were calcined at 1100 °C for 5 h in air. After furnace cooling, the

---

a)Author to whom correspondence should be addressed. Electronic mail: dylu@jlict.edu.cn

calcined mixtures were reground. Aqueous PVA (polyvinyl alcohol) solution was added into the calcined mixtures. The resulting powders were pressed uniaxially at 200 MPa into disk-like pellets of 12 mm in diameter. The discs were placed in a pile on the bottom of the Al_2O_3 crucible in an electric furnace. The discs were heated at a rate of 100 °C h^{-1} and sintered at 1400 °C for 12 h in air, cooled at a rate of −200 °C h^{-1} to 700 °C, and then furnace cooled to room temperature (RT) to form ceramics. In addition, $BaCeO_3$, $BaTbO_3$, $SrCeO_3$, and $SrTbO_3$ ceramics were prepared under the same conditions as BSTC.

B. X-ray powder diffraction

Diffraction data were collected at RT on a DX-2700 X-ray diffractometer (Dandong Haoyuan), with the Bragg–Brentano geometry, using Cu$K\alpha$ radiation ($\lambda = 1.5418$ Å) with 35 kV and 30 mA, divergence slit of 1°; anti-scatter slit of 1°; receiving slit of 0.3 mm. The diffraction pattern was scanned between $5° \leq 2\theta \leq 120°$ in 0.02° 2θ intervals with a fixed-time counting of 3 s $step^{-1}$.

The Rietveld refinements were used to refine the crystal structure. The peak shape was described by a pseudo-Voigt function. The starting data needed for Rietveld refinements for BSTC1 and BSTC3/2 are the atomic positions and unit-cell parameters from $BaCeO_3$ (88592-ICSD) and $SrCeO_3$ (PDF#01-074-8250), respectively.

C. Scanning electron microscopy, backscattered electron, and energy-dispersive X-ray spectroscopy

Microstructures of polished and thermally etched ceramic surfaces were examined using an EVOMA 10 scanning electric microscope (SEM) (Zeiss) operated at 15 kV. To confirm the nature of single phase and the absence of secondary phases in BSTC, SEM investigations in the backscattered electron (BSE) mode were performed. Aztec 2.3 energy-dispersive X-ray (EDX) spectrometer (Oxford, UK) was attached to the SEM for compositional analyses.

D. Electrical measurements

Both surfaces of polished ceramic disks (10 mm in diameter and 0.8 mm in thickness) were sputtered with Au and silver paste to form electrodes for electric measurements. Temperature dependences of the electrical conductivity (σ), the dielectric permittivity (ϵ'), and the dielectric loss (tan δ) at a frequency of 1 kHz were measured from −75 to 200 °C at a heating rate of 2 °C min^{-1} using a Concept 41 Dielectric/Impedance spectrometer (Novocontrol) with an applied voltage of 1 V. Frequency dependences of σ, ϵ', and tan δ were measured at RT. The accuracy in measurements of ϵ', tan δ, and temperature control is less than 5%, 3 × 10^{-5}, and ±0.3 °C, respectively.

E. Electron paramagnetic resonance

EPR spectra were measured using an A300 electron-spin resonance spectrometer system (Bruker BioSpin GMBH) at an X-band frequency of 9.148 GHz. The EPR of six samples, (1) 1 mg of $BaTbO_3$ + 99 mg of $BaCeO_3$, (2) 1 mg of $SrTbO_3$ + 99 mg of $SrCeO_3$, (3) 5 mg of BSTC1 + 95 mg of $BaCeO_3$,

(4) 5 mg of BSTC3/2 + 95 mg of $BaCeO_3$, (5) 100 mg of $BaCeO_3$, and (6) 100 mg of $SrCeO_3$, were measured at RT. The g-factor is calculated by the formula $h\nu_0 = g\beta H$, where the Planck's constant is $h = 6.0626 \times 10^{-34}$ J s, ν_0 is the frequency, $\beta = 9.262 \times 10^{-24}$ J T^{-1}, and H is the magnetic field strength.

F. X-ray photoelectron spectroscopy

XPS measurements were performed at RT using an Escalab 250 Xi X-ray photoelectron spectrometer (Thermo Electron). XPS raw data were processed by smoothing multiple times. The core-level binding energy was calibrated using the C 1s peak located at 285 eV.

III. RESULTS AND DISCUSSION

A. Structure determination

For X-ray powder diffraction (XRPD) measurements, two factors are considered: (1) in general cases, the high-angle upper-limit $2\theta_m$ is taken to be 120° or larger, which is apt to yield satisfactory refined results in the crystal structure refinement (Chen *et al.*, 1995) and (2) the possible ordering of Ba^{2+}/Sr^{2+} at the A-sites or Ce/Tb at the B-sites in the lattice will result in extra peaks, forming a so-called superstructure. The superstructure peaks with higher intensity are easier to be observed in the lower 2θ range of 10–20°, such as for A-site-ordered perovskites $(Li_{1/2}Nd_{1/2})TiO_3$ (Takahashi *et al.*, 1991) and $(La_{1/2}Na_{1/2})TiO_3$ (Ioshiyuki *et al.*, 1992), as well as B-site-ordered perovskites Pb_2CaTeO_6 (Artner and Weil, 2019), Ba_2CaMoO_6 (Nguyen *et al.*, 2019), and $Ba_{2-x}La_xFeMoO_6$ (Hussain *et al.*, 2019). For these two factors, the 2θ ranges in XRPD spectra of BSTC1 and BSTC3/2 are expanded from 5° to 120° and no diffraction peaks between 5° and 20° were observed. Their XRPD patterns (black line) show perovskite-like diffraction feature, as shown in Figure 1. On the basis of the trigonal $BaCeO_3$ (88592-ICSD) and the orthorhombic $SrCeO_3$ (PDF# 01-074-8250), the XRPD patterns of BSTC1 and BSTC3/2 can be refined by the Rietveld method, and their crystalline structures are indexed as a trigonal perovskite structure with the space group R-3c and an orthorhombic perovskite structure with the space group $Pmcn$, respectively. Table I gives the details of Rietveld refinements including lattice parameters, cell volumes, crystal system, space group, reliability factors (R_p and R_{wp}), and Uiso parameters. Table II gives positional parameters and occupancy at RT. The general formulas of BSTC1 and BSTC3/2 are expressed by $Ba_2SrTb_2CeO_9$ and $Ba_{1.5}Sr_{1.5}Tb_{1.5}Ce_{1.5}O_9$, respectively. Pure phases were obtained for these two compositions, as no secondary crystalline phase was detected in the measured XRD patterns.

Under the current measuring conditions, no superstructure peaks were detected for BSTC. However, the superstructure may be imperceptible based on the XRPD, and the potential ordering in the structure is possibly undetectable by XRD. A long-time record of diffraction data benefits observations of superstructure peaks (Chen *et al.*, 1997). In order to investigate the possible ordering of Ba^{2+}/Sr^{2+} at the A-sites or Ce/Tb at the B-sites in BSTC, the XRPD spectra of both samples were measured between $5° \leq 2\theta \leq 20°$ in smaller 2θ intervals (0.01°) with a slow counting of 6 s $step^{-1}$ (not presented here).
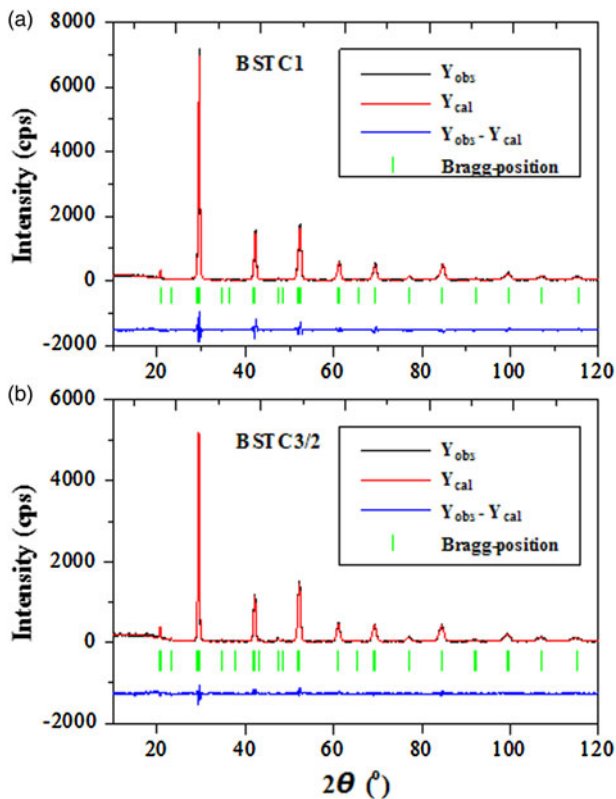
Figure 1. (Colour online) Final Rietveld plots for (a) BSTC1 and (b) BSTC3/2 ceramics. The upper patterns illustrate the observed data (black line) and the calculated pattern (red line). The vertical green markers show the calculated positions of Bragg reflections. The lower blue curve is the difference diagram.

Extra peaks were not observed. Thus, Ba^{2+}/Sr^{2+} at the A-sites or Ce/Tb at the B-sites in the perovskite lattice are considered to be randomly disordered (Chen *et al.*, 1989, 1995; Ioshiyuki *et al.*, 1992; Sahoo *et al.*, 2016); their ordering is very weak if existed (Chen *et al.*, 1997). BSTC1 and BSTC3/2 can be thought to possess disordered perovskite structures.

The four ceramic phases prepared according to the same conditions as BSTC for structural and valence state analyses. The observed and simulated XRPD patterns of $BaCeO_3$, $BaTbO_3$, $SrCeO_3$, and $SrTbO_3$ are shown in Figure 2. $BaCeO_3$, $SrCeO_3$, and $SrTbO_3$ exhibit orthorhombic perovskite structures, corresponding to PDF# 01-070-6741, PDF# 01-074-8250, and PDF# 01-089-5513, respectively, whereas $BaTbO_3$ has a tetragonal structure (PDF# 01-074-4289).

B. Microstructure and evidence of single phase

The BSE and SEM images, as well as EDX spectra for BSTC1 and BSTC3/2, are shown in Figure 3. Both samples show nonuniform microstructures with a grain size distribution from 0.2 to 3 μm, but they are denser. Their relative density (ρ_r), which is referred to as the ratio of the volumetric mass density to the theoretical density (Lu *et al.*, 2019), was determined to be 93%. This reveals that dual doping with Sr and Tb in $BaCeO_3$ is apt to the densification of ceramics.

On the basis of BSE investigations, no difference in brightness was observed for all of the grains, suggesting the absence of secondary phases in BSTC. To further clarify the single-phase nature of BSTC, EDX investigations were made to provide evidence for compositional distributions in different grains and grain boundaries. For BSTC1, the ratios of Ba to Sr and Tb to Ce at a fine grain, a triple-grain boundary, and a coarse grain are 2.0–2.1 and 1.8–2.0, respectively, which are close to the theoretical values of Ba/Sr = Tb/Ce = 2. Similarly, the ratios of Ba/Sr = 0.9–1.0 and Tb/Ce = 0.8–1.0 for BSTC3/2 are also close to the theoretical value of Ba/Sr = Tb/Ce = 1. These EDXS results reveal the homogeneous concentration distributions of Ba, Sr, Tb, and Ce in BSTC. That is to say, Ba/Sr and Tb/Ce are completely incorporated into the A-sites and the B-sites in the BSTC perovskite lattice, respectively, and no secondary phase is present; both BSTC1 and BSTC3/2 are single-phase solutions. Figure 4 gives the schematic diagram of the crystal structure for BSTC1 as a representative.

C. Electrical properties

Figure 5 shows a plot of the electrical conductivity (σ) as a function of temperature (T) at 1 kHz for BSTC1 and BSTC3/2. The σ increases rapidly with increasing T. When $T = 197$ °C, the σ value of BSTC1 ($\sigma = 5.8 \times 10^{-6}$ S cm^{-1}) is slightly greater than that of BSTC3/2 ($\sigma = 4.5 \times 10^{-6}$ S cm^{-1}). This reveals that the difference in x has only a minor effect on the electrical conductivity of both samples. The σ at 25 °C increases slowly with increasing frequency (f), as shown in Figure 5 inset, which suggests that hole conduction is predominant, rather than electron conduction.

Figure 6 shows the temperature dependences of the dielectric permittivity (ϵ') at 1 kHz and the dielectric loss (tan δ) at RT for BSTC1 and BSTC3/2. Both ϵ' and tan δ at 1 kHz increase rapidly with increasing T because of high electrical conducting behavior. This further confirms that BSTC1 and BSTC3/2 are semiconductors.

TABLE I. Details of Rietveld refinements for $Ba_2SrTb_2CeO_9$ and $Ba_{1.5}Sr_{1.5}Ce_{1.5}Tb_{1.5}O_9$ perovskites at RT.

Composition	$Ba_2SrTb_2CeO_9$	$Ba_{1.5}Sr_{1.5}Ce_{1.5}Tb_{1.5}O_9$
Wavelength (Å)	$\lambda_1 = 1.54056$ (Cu$K\alpha_1$)	$\lambda_1 = 1.54056$ (Cu$K\alpha_1$)
	$\lambda_2 = 1.54439$ (Cu$K\alpha_2$)	$\lambda_2 = 1.54439$ (Cu$K\alpha_2$)
2θ step scan increment (°)	0.02	0.02
2θ range (°)	10–120	10–120
Profile function	Pseudo-Voigt	Pseudo-Voigt
Crystal system	Trigonal	Orthorhombic
Space group	R-$3c$	$Pmcn$
a (Å)	6.0531(3)	8.5665(6)
b (Å)	6.0531	6.0651(6)
c (Å)	6.0531	6.1016(6)
V_0 (Å^3)	157.86(1)	317.02(2)
α	60.2918(28)	90.00
β	60.2918	90.00
γ	60.2918	90.00
R_p	9.92%	7.78%
R_{wp}	11.99%	9.69%
χ^2	2.304	1.847
Z	6	12
Uiso(Ba)	0.01306	0.00168
Uiso(Sr)	0.01306	0.00168
Uiso(Tb)	0.01204	0.00186
Uiso(Ce)	0.01204	0.00186
Uiso(O)	0.03262	0.01326
		0.01688

TABLE II. Positional parameters and occupancy for Ba$_2$SrTb$_2$CeO$_9$ (BSTC1) and Ba$_{1.5}$Sr$_{1.5}$Ce$_{1.5}$Tb$_{1.5}$O$_9$ (BSTC3/2) perovskites at RT.

Atom	x	y	z	Occupancy	Site symmetry	Z
BSTC1						6
Ba	0.25	0.25	0.25	0.6667	2	
Sr	0.25	0.25	0.25	0.3333	2	
Ce	0	0	0	0.3333	2	
Tb	0	0	0	0.6667	2	
O1	0.8134	0.6866	0.25	1	6	
BSTC3/2						12
Ba/Sr	0.25	0.0143	−0.0338	0.5	4	
Ce/Tb	0	0.5	0	0.5	4	
O1	0.25	0.549	0.0029	1	4	
O2	−0.0425	0.7028	0.3007	1	8	

D. EPR investigations

The EPR technique can gather an insight into the valence state of rare-earth ions and vacancies in ceramics (Lu, 2015; Lu *et al*., 2016a). The EPR spectra of BaCeO$_3$, SrCeO$_3$, BaTbO$_3$, SrTbO$_3$, BSTC1, and BSTC3/2 at RT are shown Figure 7. Ce^{3+} ($4f^1$) Kramers ion in compounds is EPR silent at RT because of its short spin-lattice relaxation time. Ce^{4+}

($4f^0$) non-Kramers ion is also EPR silent in theory. Hence, no EPR signal was observed for BaCeO$_3$ and SrCeO$_3$.

Our experiments clarified that the EPR cannot be observed for 100 mg of samples containing Tb because of the strong EPR from Tb^{4+}. For this reason, 1 mg of BaTbO$_3$ or SrTbO$_3$ and 5 mg of BSTC1 or BSTC3/2 are dispersed into 99 and 95 mg of BaCeO$_3$ or SrCeO$_3$ for EPR observations. A very broad singlet signal at $g = 2.020$–2.029 appears in the four ceramics BaTbO$_3$, SrTbO$_3$, BSTC1, and BSTC3/2. This signal originates from Tb^{4+} ($4f^7$) Kramers ions because there is no EPR response for Ba^{2+}, Sr^{2+}, Ce^{4+}, and O^{2-}. For 5% Tb-doped BaTiO$_3$ ceramics, however, Tb^{4+}-related signal appears at $g = \sim6.5$ (Lu, 2015; Lu *et al*., 2016b). This reveals that when TbO$_6$ octahedrons act as the perovskite skeleton, the Tb^{4+}-related EPR signal exhibits different g values. Thus, the EPR investigations provide evidence of the existence of a large number of Tb^{4+} ions in BSTC1 and BSTC3/2.

For doped BaTiO$_3$ ceramics, oxygen vacancies (V$_O$) can be detected in the low-temperature rhombohedral phase of $T \leq -100$ °C (Lu *et al*., 2016c). It is reported that SrCeO$_3$ may remain orthorhombic, the space group *Pbnm* from 1.2 K up to the 1 atm melting point of 2266 K. (Knight *et al*., 2015). Our experiments confirm that no additional V$_O$-related EPR signal was observed for BSTC1 and BSTC3/2 (not presented here) because no phase transition was observed in these two ceramics.

E. XPS investigations

XPS spectra of Ce 3d and Tb 3d core levels of BSTC1, BSTC3/2, SrCeO$_3$, BaCeO$_3$, SrTbO$_3$, and Tb$_4$O$_7$ are shown in Figure 8. The Ce^{3+} and Ce^{4+} species in compounds can be differentiated by XPS, with distinct line shapes corresponding to various final states: Ce(III) = $v_0 + v' + u_0 + u'$ and Ce(IV) = $v + v'' + v''' + u + u'' + u'''$. The u''' component, as a satellite peak, is a fingerprint of Ce^{4+} state, which arises from the so-called shake-down effect (Schneider *et al*., 1981; Bêche et al., 2008; Jaiswal *et al*., 2016; Xiong *et al*., 2016). It can be seen from Figure 8(a) that the Ce 3$d_{3/2}$ and Ce 3$d_{5/2}$ photoelectron lines of all Ce-containing samples exhibit the characteristic features of tetravalent cerium, in good agreement with the reports from other authors (Braaten *et al*., 1989; Douillard *et al*., 1994; Bêche et al., 2008). The final states corresponding to core-level binding energy are as follows: Ce 3$d^9 4f^0$ O 2p^6 final state: $u''' = 916.3 \pm 0.1$ eV, $v''' = 897.9 \pm 0.1$ eV; Ce 3$d^9 4f^2$ O 2p^4 final state: $u = 900.4 \pm 0.2$ eV, $v = 882.4 \pm 0.2$ eV; Ce 3$d^9 4f^1$ O 2p^5 final state: $u'' = 907.0 \pm$
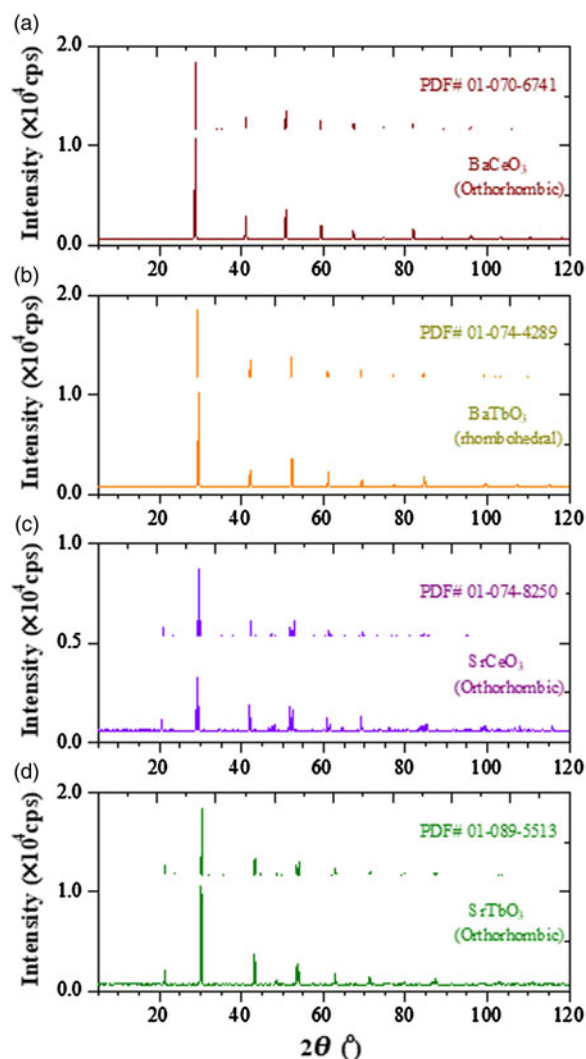

Figure 2. (Colour online) Observed and simulated XRPD patterns of (a) BaCeO$_3$, (b) BaTbO$_3$, (c) SrCeO$_3$, and (d) SrTbO$_3$.
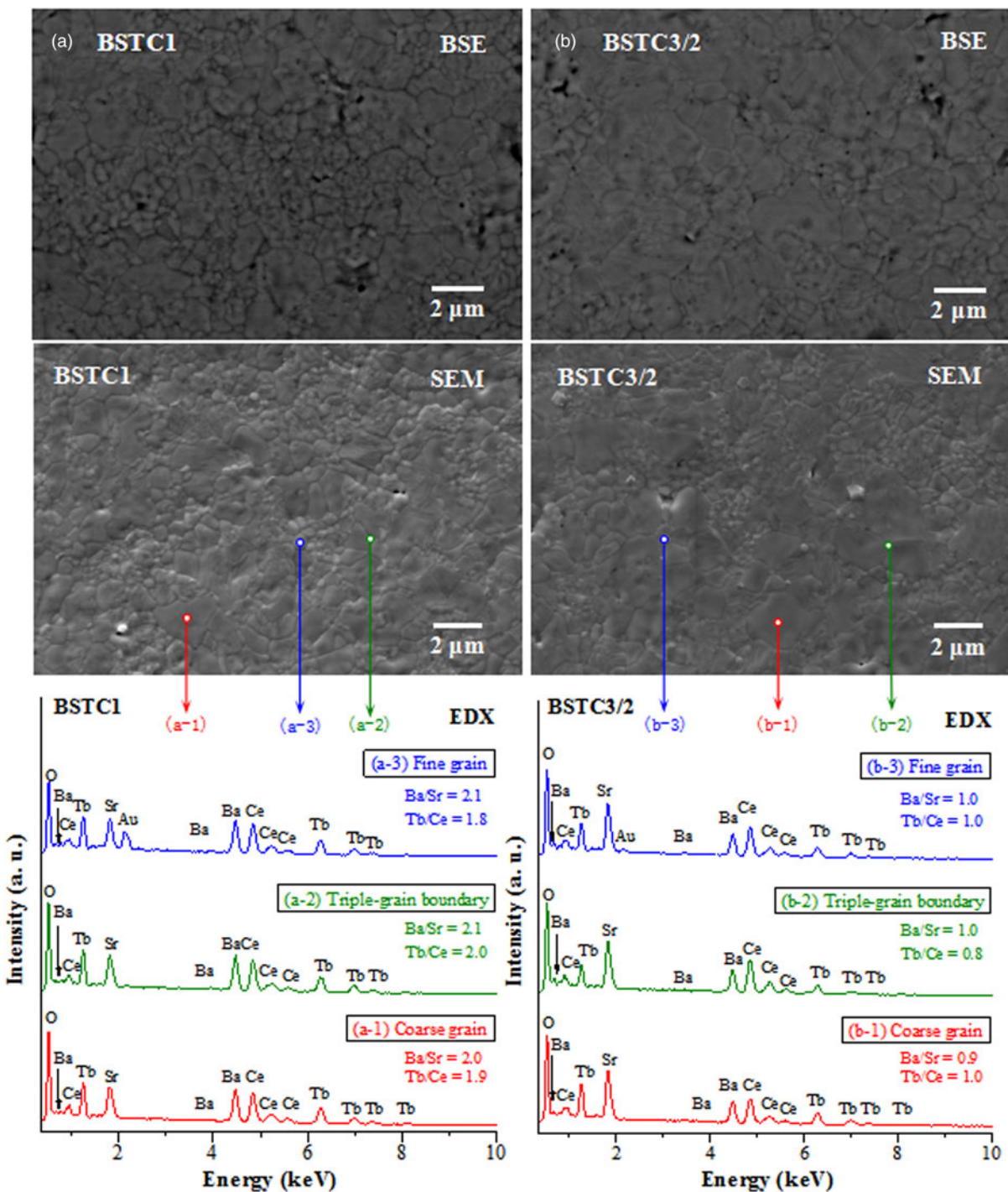
Figure 3. (Colour online) BSE and SEM images of the polished and thermally etched surfaces as well as corresponding EDX investigations at a fine grain, a triple-grain boundary junction, and a coarse grain for (a) BSTC1 and (b) BSTC3/2 ceramics.

0.3 eV, $v'' = 888.1 \pm 0.1$ eV; The Ce^{3+} spectrum (Blanco *et al.*, 2002; Bêche et al., 2008; Jaiswal *et al.*, 2016; Xiong *et al.*, 2016; Liang, 2019) is absent for BSTC. Thus, Ce is considered to be present in the form of Ce^{4+} and Ce^{3+} is negligible in BSTC1 and BSTC3/2.

For terbium ions in compounds, the most intense photoemission peak corresponds to the $3d$ core level, peaking at ~1277 eV for Tb $3d_{3/2}$ and ~1242 eV for Tb $3d_{5/2}$, respectively (Van Den Bossche *et al.*, 1994; Cao et al., 2010; Blanco *et al.*, 2002). Tb^{3+} and Tb^{4+} due to their $3d$-spectrum overlapping cannot be clearly identified. However, the core-

level spectrum of Tb^{4+} was reported to show relatively intense $3d$ satellites with binding energy ca. 10 eV higher than those of the main peaks (Van Den Bossche *et al.*, 1994; Martínez-Arias *et al.*, 2005; Blanco *et al.*, 2002), but no $3d$ satellite of Tb^{3+} is present, as observed for TbF_3 with Tb^{3+} (Van Den Bossche *et al.*, 1994).

All XPS spectra of BSTC1, BSTC3/2, $SrTbO_3$, and Tb_4O_7 show two Tb $3d$ binding energy peaks at 1276.7 ± 0.1 and 1242.1 ± 0.1 eV [Figure 8(b)], as mentioned above. A clear satellite at 1253.3 ± 0.1 eV confirms the existence of Tb^{4+} in these ceramics. The intensity of this satellite for
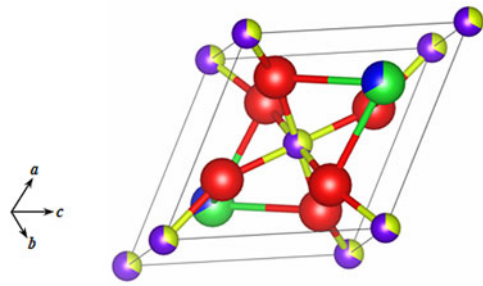
Figure 4. (Colour online) A schematic diagram of the trigonal crystal structure for BSTC1. Red balls stand for O^{2-} ions. Ba^{2+} and Sr^{2+} ions are represented by green/blue balls, whose surface consists of 2/3 green and 1/3 blue, representing the molar ratio of $Ba^{2+}/Sr^{2+} = 2:1$. Tb and Ce ions by purple/yellow balls, and the corresponding colors reflect the molar ratio of Tb/Ce = 2:1.

Figure 6. (Colour online) Temperature dependence of ϵ' at 1 kHz for BSTC1 and BSTC3/2. The inset in (a) depicts $\tan \delta$ versus T.

$SrTbO_3$ is obviously higher than the other three samples, which arises from the following two evidences: (1) the molar concentration of Tb in $SrTbO_3$ is highest and (2) the high electrical conductivity (Figure 5) should be accompanied by oxygen vacancies, which are caused by some Tb^{3+} ions in BSTC.

F. Discussion on the structure, valence states of Tb and Ce ions, and defect chemistry

For BSTC1 and BSTC3/2, the EPR and XPS results provide evidence of the existence of Tb^{4+} (Figures 7 and 8), whereas the XPS results indirectly confirm the existence of some Tb^{3+} ions at the B-sites (Figure 8). Table III gives ionic radii versus coordinate number (CN) (Shannon, 1976; Lu, 2015). For perovskite, the reduplicative orientations by BO_6 octahedron form the skeleton of the perovskite lattice and the A-site ions locate on the interstitial space of BO_6 skeleton. More stable Ce^{4+} at the B-sites in BSTC cannot be reduced to Ce^{3+} because of the existence of Tb^{4+} ions. The unit-cell volume (V_0) of the orthorhombic BSTC3/2 ($V_0 = 317.02$ Å^3) is nearly the same as that of the orthorhombic $SrCeO_3$ ($V_0 = 317.47$ Å^3) reported (Ranlov et $al.$, 1995). On the basis of the orthorhombic $SrCeO_3$ lattice, dual doping

with Ba and Tb results in only a little change in V_0. This is because the expansion in V_0 caused by the A-site Ba^{2+} ions is close to the contraction in V_0 caused by the B-site Tb^{4+} ions on the basis of ionic size comparisons between Ba^{2+} and Sr^{2+} as well as between Tb^{4+} and Ce^{4+}. The V_0 of the orthorhombic BSTC3/2 ($V_0 = 317.02$ Å^3) is evidently greater than the volume of two unit cells of the trigonal BSTC1 ($2V_0 = 315.72$ Å^3) (see Table I), which arises from the higher Ce concentration at the B-sites in BSTC3/2.

The cation and vacancy defects in BSTC based on the $SrCeO_3$ lattice can be expressed by $Ba_{Sr}^{\times}$, $Sr_{Sr}^{\times}$, $Ce_{Ce}^{\times}$, $Tb_{Ce}^{\times}$, Tb'_{Ce}, and O vacancies ($V_O^{\bullet\bullet}$). Tb ions at the B-sites in perovskites are confirmed to coexist in the form of the mixed-valence states of Tb^{3+}/Tb^{4+} (Lu, 2015; Lu and Peng, 2016; Lu et $al.$, 2016a). The higher values in the electrical conductivity (Figure 5) and the dielectric loss (Figure 6) arise from the creation of oxygen vacancies, which are compensated by some Tb^{3+} ions at the B-sites based on a general
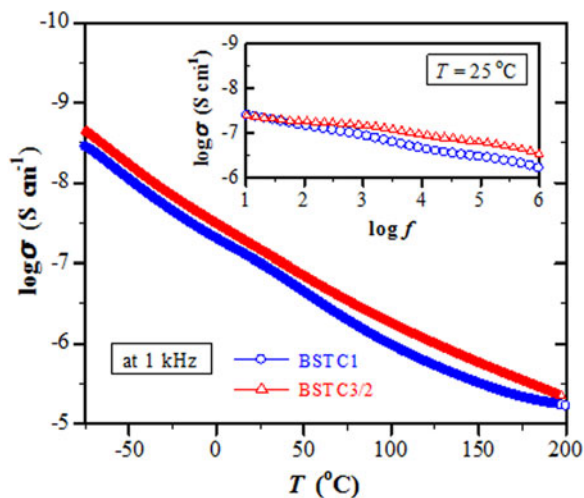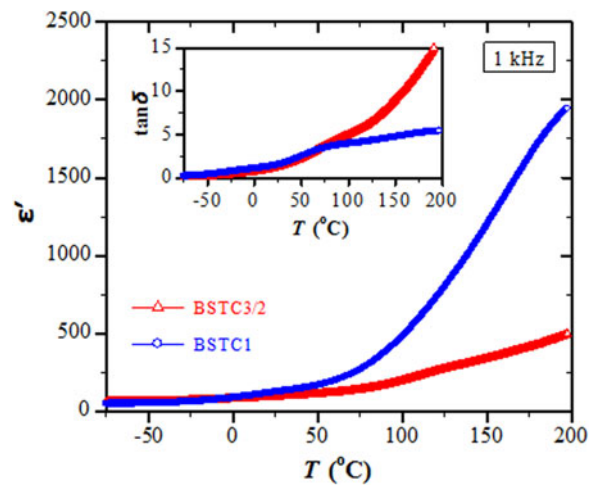

Figure 5. (Colour online) Plot of the electrical conductivity (σ) as a function of temperature for (a) BSTC1 and (b) BSTC3/2 ceramics, measured at 1 kHz. The inset depicts σ versus f at 25 °C.
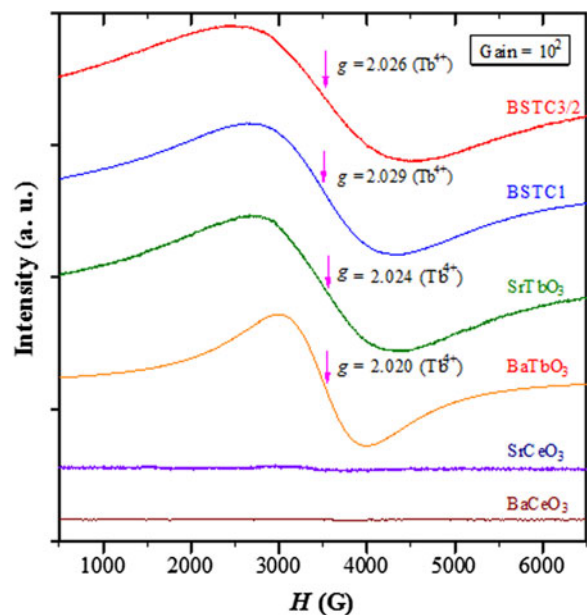

Figure 7. (Colour online) EPR spectra of $BaCeO_3$, $SrCeO_3$, $BaTbO_3$, $SrTbO_3$, BSTC1, and BSTC3/2.
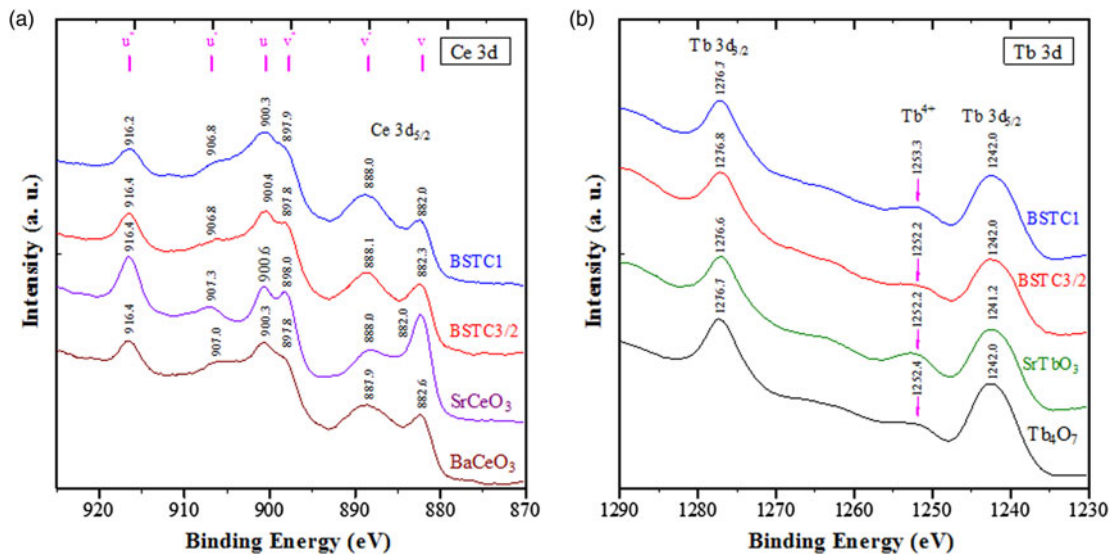
Figure 8. (Colour online) XPS spectra corresponding to (a) Ce 3*d* core levels of BSTC1, BSTC3/2, SrCeO$_3$, BaCeO$_3$ and (b) Tb 3*d* core levels of BSTC1, BSTC3/2, SrTbO$_3$, Tb$_4$O$_7$.

lattice electroneutrality condition. The sixfold coordinated Tb^{3+} can coexist with Tb^{4+} and Ce^{4+} because of a complementary ionic radii relation $2R_{Ce(IV)} \approx R_{Tb(IV)} + R_{Tb(III)}$ (Table III).

$$4BaO + Tb_4O_7 \rightarrow 4Ba_{Ba}^{\times} + 2Tb_{Ce}^{\times} + 2Tb'_{Ce} + 11O_O + V_O^{\bullet\bullet} \quad (1)$$
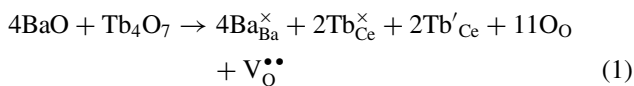
The tolerance factor (t) of ABO$_3$-type perovskite is expressed by the following equation:

$$t = \frac{r_A + r_O}{\sqrt{2}(r_B + r_O)} \quad (2)$$

where r_A, r_B, and r_O are the ionic radii of the cation A, B, and the anion O^{2-}, respectively. The ideal perovskite without distortion should show $t = 1.0$, and the t value of most perovskite-type oxides is empirically in the range of 0.75–1.0 (Fu *et al.*, 2014). For Ba$_{1-x/3}$Sr$_{x/3}$Tb$_{1-x/3}$Ce$_{x/3}$O$_3$ (BSTC), the tolerance factor may be approximately expressed by the following equation:

$$t = \frac{[(1 - x/3)r_{Ba} + x/3 \cdot r_{Sr}] + r_O}{\sqrt{2}\{[(1 - x/3)r_{Tb} + x/3 \cdot r_{Ce}] + r_O\}} \quad (3)$$

The tolerance factors of BSTC1 and BSTC3/2 are determined to be $t = 0.956$ and 0.939, respectively. These high t values show that the two BSTC phases are both nearly free of distortion of the perovskite structure.

TABLE III. Ionic radii versus coordinate number (CN).

Ions	CN	r (Å)
Ba^{2+}	12	1.61
Sr^{2+}	12	1.44
Tb^{3+}	12	1.203
Tb^{3+}	6	0.923
Tb^{4+}	6	0.76
Ce^{4+}	6	0.87
Ce^{3+}	12	1.34

IV. CONCLUSIONS

Two ceramics Ba$_{1-x/3}$Sr$_{x/3}$Tb$_{1-x/3}$Ce$_{x/3}$O$_3$ ($x = 1$ and 1.5) (BSTC) with dense microstructures ($\rho_r = 93\%$, GS = 0.2–3 μm) were prepared at 1400 °C in air using the mixed-oxides method. Dual doping with Sr and Tb in the BaCeO$_3$ perovskite results in a trigonal structure for BSTC1 and an orthorhombic perovskite structure for BSTC3/2. Ba/Sr ions at the A-sites and Ce/Tb ions at the B-sites in the perovskite lattice are randomly disordered and exhibit homogeneous concentration distributions. The EPR, XPS, and electrical results confirm that Ce and Tb ions in BSTC exist as Ce^{4+} and the mixed-valence state of Tb^{4+}/Tb^{3+}, respectively. At RT, two BSTC ceramics exhibit a similar semiconducting behavior, and the difference in x had little effect on their σ–T relations. The electrical conductivity (σ) of BSTC with $x = 1.5$ increases rapidly from 5.7×10^{-9} to 4.5×10^{-6} S cm^{-1} with increasing T from -50 to 200 °C, while the σ at RT increases slowly with increasing frequency, from 3.0×10^{-8} at 1 Hz to 2.9×10^{-7} S cm^{-1} at 10^6 Hz. Direct evidence of Tb^{3+}, oxygen vacancies, and possible local ordering still need to be further explored.

Artner, C., and Weil, M. (**2019**). "Lead(II) oxidotellurates(VI) with double perovskite structures," J. Solid State Chem. **276**, 75–86.

Barison, S., Battagliarin, M., Cavallin, T., Doubova, L., Fabrizio, M., Mortalò, C., Boldrini, S., Malavasic, L., and Gerbasid, R. (**2008**). "High conductivity and chemical stability of BaCe$_{1-x-y}$Zr$_x$Y$_y$O$_{3-\delta}$ proton conductors prepared by a sol–gel method," J. Mater. Chem. **18**, 5120–5128.

Bêche, E., Charvin, P., Perarnau, D., Abanades, S., and Flamant, G. (**2008**). "Ce 3d XPS investigation of cerium oxides and mixed cerium oxide (Ce$_x$Ti$_y$O$_z$)," Surf. Interface Anal. **40**, 264–267.

Blanco, G., Pintado, J. M., Bernal, S., Cauqui, M. A., Corchado, M. P., Galtayries, A., Ghijsen, J., Sporken, R., Eickhoff, T., and Drube, W. (**2002**). "Influence of the nature of the noble metal (Rh,Pt) on the low-

temperature reducibility of a Ce/Tb mixed oxide with application as TWC component," Surf. Interface Anal. **34**, 120–124.

Braaten, N. A., Grepstadt, J. K., and Raaen, S. (**1989**). "Effects of thin cerium overlayers on the oxidation of tantalum and aluminium," Surf. Sci. **222**, 499–516.

Cao, Y. P., Shi, F., Xiu, X. W., Sun, H. B., Guo, Y. F., Liu, W. J., and Xue, C. S. (**2010**). "Syntheses and properties of Tb-doped GaN nanowires," Inorg. Mater. **46**(10), 1096–1099.

Chen, J., Chan, H. M., and Harmer, M. P. (**1989**). "Ordering structure and dielectric properties of undoped and La/Na-doped $Pb(Mg_{1/3}Nb_{2/3})O_3$," J. Am. Ceram. Soc. **74**, 593–598.

Chen, X. L., Liang, J. K., and Wang, C. (**1995**). "Effect of high-angle diffraction data on Rietveld structure refinement," Acta Phys. Sin. (Overseas Ed.) **4**, 259–261.

Chen, X. L., Bauernfeind, L., and Braun, H. F. (**1997**). "$Na_{0.5}La_{0.5}RuO_3$: structure and electric properties," Phys. Rev. B **55**(11), 6888–6894.

Choi, S. M., Lee, J.-H., An, H., Hong, J., Kim, H., Yoon, K. J., Son, J.-W., Kim, B.-K., Lee, H.-W., and Lee, J.-H. (**2014**). "Fabrication of anode-supported protonic ceramic fuel cell with $Ba(Zr_{0.85}Y_{0.15})O_{3-\delta}$–Ba$(Ce_{0.9}Y_{0.1})O_{3-\delta}$ dual-layer electrolyte," Int. J. Hydrog. Energy **39**, 12812–12818.

Dahl, P. I., Haugsrud, R., Lea Lein, H., Grande, T., Norby, T., and Einarsrud, M.-A. (**2007**). "Synthesis, densification and electrical properties of strontium cerate ceramics," J. Eur. Ceram. Soc. **27**, 4461–4471.

Douillard, L., Gautier, M., Thromat, N., Henriot, M., and Guittet, M. J. (**1994**). "Local electronic structure of Ce-doped Y_2O_3: an XPS and XAS study," Phys. Rev. B **49**(23), 43–51.

El Hachmi, A., Tamraoui, Y., Manoun, B., Haloui, R., Elaamrani, M. A., Saadoune, I., Bih, L., and Lazor, P. (**2018**). "Synthesis and Rietveld refinements of new ceramics $Sr_2CaFe_2WO_9$ and $Sr_2PbFe_2TeO_9$ perovskites," Powder Diffr. **33**(2), 134–140.

Fu, Y.-P., and Weng, C.-S. (**2014**). "Effect of rare-earth ions doped in $BaCeO_3$ on chemical stability, mechanical properties, and conductivity properties," Ceram. Int. **40**, 10793–10802.

Hussain, I., Khan, S. N., Rao, T. N., Kumar, A., and Koo, B. H. (**2019**). "Structural, magnetic and magnetocaloric properties of double perovskites $Ba_{2-x}La_xFeMoO_6$," Solid State Sci. doi:10.1016/j.solidstatesciences.2019.105991.

Ioshiyuki, Y., Sohn, J.-H., Kim, I.-S., Itoh, M., and Nakamura, T. (**1992**). "Quantum paraelectricity in a perovskite $La_{1/2}Na_{1/2}TiO_3$," J. Phys. Soc. Jpn. **61**(10), 3831–3832.

Iwahara, H., Asakura, Y., Katahira, K., and Tanaka, N. (**2004**). "Prospective of hydrogen technology using proton-conducting ceramics," Solid State Ion. **168**, 299–310.

Jaiswal, S. K., Hong, J., Yoon, K. J., Son, J. W., Lee, H. W., and Lee, J. H. (**2016**). "Optical absorption and XPS studies of $(Ba_{1-x}Sr_x)(Ce_{0.75}Zr_{0.10}Y_{0.15})O_{3-\delta}$ electrolytes for protonic ceramic fuel cells," Ceram. Int. **42**, 10366–10372.

Kannan, R., Gill, S., Maffei, N., and Thangadurai, V. (**2013**). "$BaCe_{0.85-x}Zr_xSm_{0.15}O_{3-\delta}$ (0.01 0.3) (BCZS): effect of Zr content in BCZS on chemical stability in CO_2 and H_2O vapor, and proton conductivity," J. Electrochem. Soc. **160**, 18–26.

Knight, K. S., Haynes, R., Bonanos, N., and Azough, F. (**2015**). "Thermoelastic and structural properties of ionically conducting cerate perovskites: (II) $SrCeO_3$ between 1273 K and 1723 K," Dalton Trans. **44**(23), 10773–10784.

Liang, P. (**2019**). "Co-existence phenomenon of Ce^{3+}/Ce^{4+} and Tb^{3+} in Ce/Tb co-doped $Zn_2(BO_3)(OH)_{0.75}F_{0.25}$ phosphor: luminescence and energy transfer," Adv. Powder Technol. **30**, 974–982.

Lu, D. (**2015**). "Self-adjustable site occupations between Ba-site Tb^{3+} and Ti-site Tb^{4+} ions in terbium-doped barium titanate ceramics," Solid State Ion. **276**, 98–106.

Lu, D., and Peng, Y. (**2016**). "Dielectric properties and exploration of self-compensation mode of Tb in $BaTiO_3$ ceramics," J. Ceram. Soc. Jpn. **124**(4), 455–459.

Lu, D., Cui, S., Liu, Q., and Sun, X. (**2016a**). "Dielectric properties and defect chemistry of barium titanate ceramics co-doped R and Dy ions (R= Eu, Gd, Tb)," Ceram. Int. **42**(13), 14364–14373.

Lu, D., Peng, Y., Yu, X., and Sun, X. (**2016b**). "Dielectric properties and defect chemistry of La and Tb co-doped $BaTiO_3$ ceramics," J. Alloy. Compd. **681**, 128–138.

Lu, D., Yuan, L., Liang, W., and Zhu, Z. (**2016c**). "Characterization of oxygen vacancy defects in $Ba_{1-x}Ca_xTiO_3$ insulating ceramics using electron para-magnetic resonance technique," Jpn. J. Appl. Phys. **55**, 011501.

Lu, D., Gao, X., and Wang, S. (**2019**). "Abnormal Curie-temperature shift in Ho-doped $BaTiO_3$ ceramics with the self-compensation mode," Res. Phys. **12**, 585–591.

Malavasi, L., Ritter, C., and Chiodelli, G. (**2008**). "Correlation between thermal properties, electrical conductivity and crystal structure in the $BaCe_{0.80}Y_{0.20}O_{2.9}$ proton conductor," Chem. Mater. **20**, 2343–2351.

Martínez-Arias, A., Hungría, A. B., Fernandez-García, M., Iglesias-Juez, A., Conesa, J. C., Mather, G. C., and Munuera, G. (**2005**). "Cerium–terbium mixed oxides as potential materials for anodes in solid oxide fuel cells," J. Power Sources **151**, 43–51.

Matsumoto, H., Suzuki, T., and Iwahara, H. (**1999**). "Automatic regulation of hydrogen partial pressure using a proton conducting ceramic based on $SrCeO_3$," Solid State Ion. **116**, 99–104.

Mukundan, R., Davies, P. K., and Worrell, W. L. (**2001**). "Electrochemical characterization of mixed conducting $Ba(Ce_{0.8-y}Pr_yGd_{0.2})O_{2.9}$ cathodes," J. Electrochem. Soc. **148**, 82–86.

Nguyen, L. T., Cava, R. J., and Fry-Petit, A. M. (**2019**). "Low temperature structural phase transition in the Ba_2CaMoO_6 perovskite," J. Solid State Chem. **277**, 415–421.

Radenahmad, N., Afif, A., Petra, M. I., Rahman, S. M. H., Eriksson, S., and Azad, A. K. (**2016**). "High conductivity and high density proton conducting $Ba_{1-x}Sr_xCe_{0.5}Zr_{0.35}Y_{0.1}Sm_{0.05}O_{3-\delta}$ ($x = 0.5, 0.7, 0.9, 1.0$) perovskites for IT-SOFC," Int. J. Hydrog. Energy **41**, 11832–11841.

Ranlov, J., Lebech, B., and Nielsen, K. (**1995**). "Neutron diffraction investigation of the atomic defect structure of Y-doped $SrCeO_3$, a high-temperature protonic conductor," J. Mater. Chem. **5**, 743–747.

Ricote, S., Bonanos, N., Lenrick, F., and Wallenberg, R. (**2012**). "$LaCoO_3$: promising cathode material for protonic ceramic fuel cells based on a $BaCe_{0.2}Zr_{0.7}Y_{0.1}O_{3-\delta}$ electrolyte," J. Power Sources **218**, 313–319.

Sahoo, M. P. K., Zhang, Y., and Wang, J. (**2016**). "Enhancement of ferroelectric polarization in layered $BaZrO_3/BaTiO_3$ superlattices," Phys. Lett. A **380**(1–2), 299–303.

Scherban, T., Lee, W.-K., and Nowick, A. S. (**1988**). "Bulk protonic conduction in Yb-doped $SrCeO_3$ and $BaCeO_3$," Solid State Ion. **28–30**, 585–588.

Schneider, W.-D., Laubschat, C., Nowik, I., and Kaindl, G. (**1981**). "Shake-up excitations and core-hole screening in Eu systems," Phys. Rev. B **24**, 5422–5425.

Shannon, R. D. (**1976**). "Revised effective ionic radii and systematic studies of interatomic distances in halides and chalcogenides," Acta Crystallogr. A **32**, 751–767.

Sharova, N. V., Gorelov, V. P., and Balakireva, V. B. (**2005**). "Charge transport in $BaCe_{0.85}R_{0.15}O_{3-\delta}$ (R = Sm, Pr, Tb) in oxidizing and reducing environment," Russ. J. Electrochem. **41**, 665–670.

Takahashi, H., Baba, Y., Ezaki, K., Okamoto, Y., Shibata, K., Kuroki, K., and Nakano, M. (**1991**). "Dielectric characteristics of $(A_{1/2}^{1+} \bullet A_{1/2}^{3+})TiO_3$ ceramics at microwave frequencies," Jpn. J. Appl. Phys. **30**(9), 2339–2342.

Tolchard, J., and Grande, T. (**2007**). "Physicochemical compatibility of $SrCeO_3$ with potential SOFC cathodes," J. Solid State Chem. **180**, 2808–2815.

Uchida, H., Maeda, N., and Iwahara, H. (**1983**). "Relation between proton and hole conduction in $SrCeO_3$-based solid electrolytes under water-containing atmospheres at high temperatures," Solid State Ion. **11**, 117–124.

Van Den Bossche, J., Neyts, K. A., De Visschere, P., Corlatan, D., Pauwels, H., Vercaemst, R., Fierman, L., Poelma, D., Van Meirhaegh, R. L., Laflere, W. H., and Cardon, F. (**1994**). "XPS study of TbF_3, and TbOF centres in ZnS," Phys. Stat. Sol. A **146**, K67–K70.

Wang, J., Li, L., Campbell, B. J., Lv, Z., Ji, Y., Xue, Y., and Sua, W. (**2004**). "Structure, thermal expansion and transport properties of $BaCe_{1-x}Eu_xO_{3-\delta}$ oxides," Mater. Chem. Phys. **86**, 150–155.

Wu, J., Li, L., Espinosa, W. T. P., and Haile, S. M. (**2004**). "Defect chemistry and transport properties of $Ba_xCe_{0.85}M_{0.15}O_{3-\delta}$," J. Mater. Res. **19**, 2366–2376.

Xiong, Z., Hua, Q., Liu, D., Wu, C., Zhou, F., Wang, Y., Jin, J., and Lu, C. (**2016**). "Influence of partial substitution of iron oxide by titanium oxide on the structure and activity of iron–cerium mixed oxide catalyst for selective catalytic reduction of NO_x with NH_3," Fuel **165**, 432–439.